

# Active Posts in Deterministic Lateral Displacement Devices

Jason P. Beech,\* Kevin Keim, Bao Dang Ho, Carlotta Guiducci, and Jonas O. Tegenfeldt\*

Using electrically connected metal-coated posts in a deterministic lateral displacement (DLD) device and applying electric fields, electrokinetics is used to tune separations, significantly decrease the critical size for separation, and increase the dynamic range with switching times on the order of seconds. The strength of DLD stems from its binary behavior. To first approximation, particles move in one out of two trajectories based on their effective size. For particles that are close to the threshold size, a small external force is sufficient to nudge the particles from one trajectory to another. The devices consist of arrays of cylindrical metal-coated SU-8 posts connected by an underlying metal layer. This allows the application of voltages at the post surfaces and the generation of electric field gradients between neighboring posts, causing polarizable particles to experience a dielectrophoretic (DEP) force. This force, which depends on the volume and polarizability of the particle, can be made sufficient to push particles from one trajectory into another. In this way, the critical size in a device, normally fixed by the geometry, can be tuned. What's more, adding DEP in this way allows for the simultaneous creation of multiple size fractions.

that no external fields or actuations other than the generation of flow are required to separate particles. "Continuous" refers to the fact that a mixture of particles can be input into the device and continuously extracted as several subpopulations from different outputs of the device in contrast to batch methods where the device needs to be restarted for each batch. The passive nature of the technique means that DLD is ideal for integration into simple devices that require little to no power input and continuity means that this can be done easily with up/down stream preparative or analytical steps. However, "passive" also means that once designed and fabricated, the separation performance of a device is fixed.

The basic principle of DLD is simple. Particles with diameters less than a threshold value, the critical diameter<sup>[2]</sup> of the device,  $D_C$ , move along the flow through the device and particles with

diameters greater than the critical diameter are displaced and move along a direction determined by the geometry of the post array (Figure 1A). The critical diameter is determined by the geometry of the post array and is therefore fixed. To introduce tunability of the separation functionality requires additional refinement. Beech and Tegenfeldt used the deformability of PDMS to change the DLD device geometry by pulling on it and thereby change the critical size of the device.<sup>[3]</sup> Zeming et al. used innate, long-range electrostatic forces inside DLD devices, modulated via buffer ionic strength, to tune separations and achieve a large reduction of the critical size.<sup>[4]</sup> Zeming et al. recently used this approach to detect the binding of proteins to the surface of micrometer-sized beads.<sup>[5]</sup> In both of the above cases, nanometer-sized particles are separated in devices with micrometer-sized features. As the authors argue, this approach delivers powerful separations in devices that are easy to fabricate (large features) and easy to run (low pressures). Most relevant to the current work, Beech et al. used electric fields to modify the behavior of polystyrene microspheres in DLD devices.<sup>[6]</sup> This approach also enables the tuning of devices and the decrease of the critical size. It requires the application of electric fields but has the advantage that tuning can be done quickly and reversibly without the need to change the buffer. These devices were simple to fabricate and use, requiring only electrodes added at the inlets and outlets of devices. The insulating properties of PDMS generate insulator-based dielectrophoretic (DEP) forces<sup>[7]</sup> that tune the separations in DLD devices. This approach has now been refined by Ho et al. (submitted for publication) who

## 1. Introduction

In many types of miniaturized integrated fluidic systems, particle sorting is essential for sample preparation and analytical fractionation. Microfluidics simplifies the process considerably compared to standard methods such as fluorescence-activated cell sorting (FACS) and magnetic-activated cell sorting (MACS). For high-throughput applications, acoustophoresis and inertial focusing have been developed. However, they provide limited precision. For high-resolution fractionation, deterministic lateral displacement (DLD) is excellent. It was first presented by Huang et al.<sup>[1]</sup> and is, in its original form, a passive and continuous particle separation technique for the separation of particles by size. "Passive" refers to the fact that separation functionality is built into the structure of the device and

Dr. J. P. Beech, Dr. B. D. Ho, Prof. J. O. Tegenfeldt  
Division of Solid State Physics and NanoLund  
Lund University  
Lund SE-221 00, Sweden  
E-mail: jason.beech@ff.lth.se; jonas.tegenfeldt@ff.lth.se

K. Keim, Prof. C. Guiducci  
Laboratory of Life Sciences Electronics  
École Polytechnique Fédérale de Lausanne  
Lausanne CH-1015, Switzerland

 The ORCID identification number(s) for the author(s) of this article can be found under <https://doi.org/10.1002/admt.201900339>.

DOI: 10.1002/admt.201900339

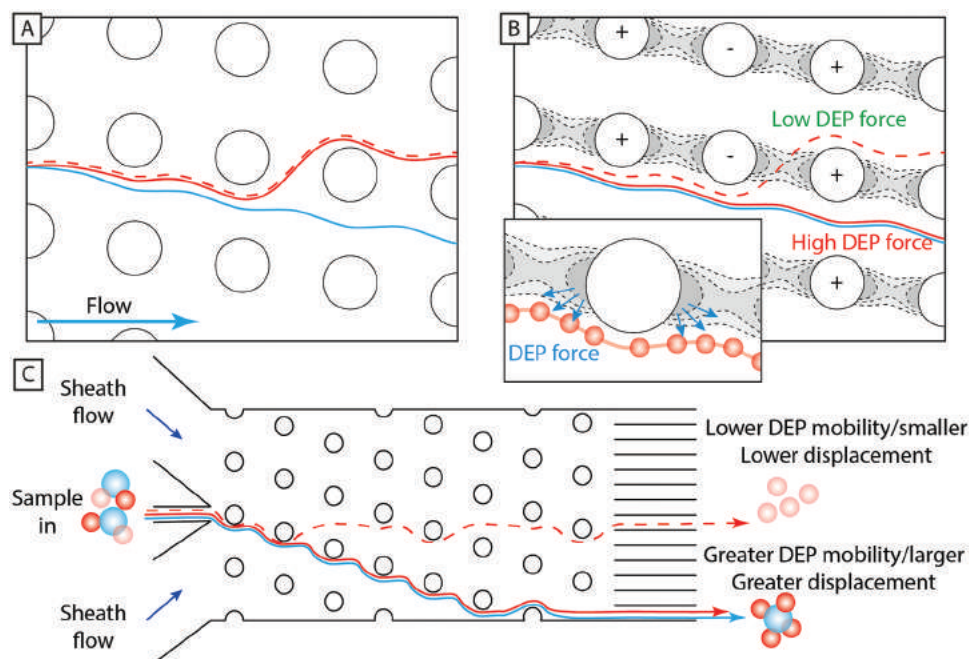


**Figure 1.** Device principle. A) Particles smaller than the critical size in a DLD device move in the zigzag mode, following the average fluid flow direction (both solid and dashed red lines) while those larger than the critical size flow in the displacement mode (blue line). B) If the posts are active electrodes, then electric fields can be generated between the rows of posts in such a way that DEP forces cause particles to transition to the displacement mode (the inset shows an illustration of the forces). C) Using this principle, devices can be designed such that particles with the same size but different DEP mobilities can be separated and subsequently collected (solid red line).

have used buffer conditions and applied voltages and frequencies to separate microspheres, bacteria, and yeast based not only on size, but on surface charge and other dielectric properties. However, generating high electric fields in devices using this approach requires high applied voltages (typically hundreds to thousands of volts), which can be problematic from a practical point of view, and it can be difficult to do this at high frequencies without specialized equipment.

Here, we present a new approach to combine DEP and DLD by fabricating post arrays that also serve as electrodes. These three-dimensional electrodes have been used previously for an

impedance flow cytometer<sup>[8a]</sup> and for parallelized electrorotation in a microfluidic channel.<sup>[8b]</sup> With our new design, we are able to generate similar field gradients as in our previous work<sup>[6]</sup> using two orders of magnitude lower applied voltages due to the proximity of the electrodes (Figures 1 and 2). This allows us to work with frequencies up to tens of megahertz using standard signal generators. Using this approach, we reversibly decrease the critical particle size in a device from 6 to 0.25  $\mu\text{m}$ , a factor of 24, equivalent to increasing the dynamic range from 1 to 24. The switching times for adjustment of critical sizes within the demonstrated range are on the order of seconds.

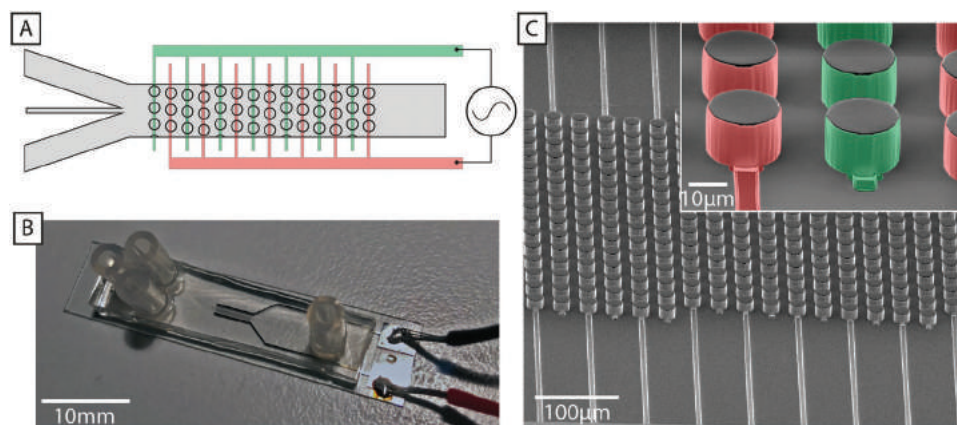


**Figure 2.** A) Schematic of device design showing how the electrodes are coupled. B) Photograph of a finished device showing inlet and outlet reservoirs and wires for fluid and electronic interfacing. C) Colorized SEM micrograph of the active post region. The posts that constitute the DLD array are coated with metal (shown in red and green) and connected via buried metal lines. The red and green colorized electrodes are connected as depicted in (A) to have opposite polarity.

## 2. Theory

### 2.1. Deterministic Lateral Displacement

The critical particle diameter  $D_C$  in a DLD array with gap  $G$  and period  $N$  can be estimated using the empirical formula<sup>[9]</sup>

$$D_C = 1.4 \cdot G \cdot N^{-0.48} \quad (1)$$

As shown in Figure S2 in the Supporting Information, the measured gap in our device,  $G = 11.10 \pm 0.14 \mu\text{m}$ . With the period designed to be  $N = 10$ , the critical particle diameter is expected to be  $D_C = 5.15 \pm 0.06 \mu\text{m}$  and is measured experimentally (Section 3 and Figure 3) to be  $\approx 6 \mu\text{m}$ .

This means that particles with diameters smaller than  $6 \mu\text{m}$  are expected to follow the fluid flow direction in the device (commonly referred to as the zigzag mode) and those larger than  $6 \mu\text{m}$  will follow the geometry of the array (bumping or displacement mode). Here, we will refer to the two modes as zigzag and displacement. Further studies have refined our understanding of DLD mechanisms<sup>[10,11]</sup> and have shown the existence of a mode that lies between the zigzag and displacement modes and that has its origins in anisotropic permeability<sup>[10,12]</sup> and broken flow symmetry.<sup>[13]</sup> We observe this mixed mode in our measurements (Figure 3), and observe how particles switch from zigzag to displacement via the mixed mode.

### 2.2. Dielectrophoresis

Dielectrophoresis provides specificity based on both the volume and the dielectric properties of the particles.

The resistance to the formation of an electric field, the complex permittivity  $\tilde{\epsilon}$ , inside a material upon the application of an external alternating field is a function of frequency,  $f$ , and is given by the following where  $\epsilon$  is the permittivity (in a static field) and  $\sigma$  is the conductivity

$$\tilde{\epsilon} = \epsilon - j \frac{\sigma}{2\pi f} \quad (2)$$

The time-averaged force  $\langle F_{\text{DEP}} \rangle$  on a spherical particle of radius  $r$  and complex permittivity  $\tilde{\epsilon}_p$  suspended in a medium with complex permittivity  $\tilde{\epsilon}_m$  and a sinusoidal electric field with an amplitude of  $E$  is given by

$$\langle F_{\text{DEP}} \rangle = \pi \epsilon_m r^3 \text{Re}(f_{\text{CM}}) \nabla E^2 \quad (3)$$

The force depends on the contrast in dielectric properties between the particle and the surrounding medium as expressed by the real part of the Clausius–Mossotti factor ( $f_{\text{CM}}$ ) (Equation (4)). This factor also carries the frequency dependence

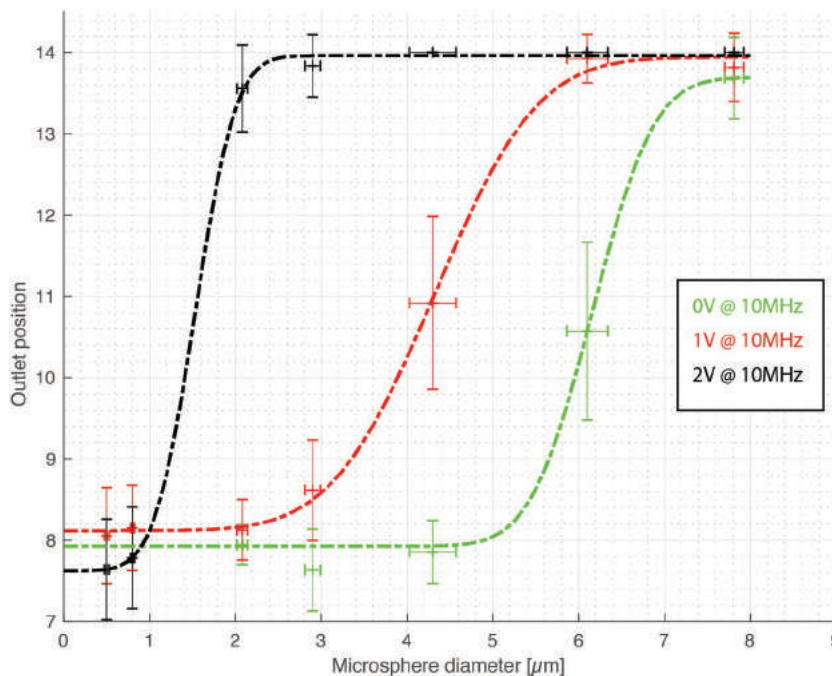


**Figure 3.** Displacement of microspheres as a function of diameter with and without applied electric field with fitted error functions. At zero applied field (green), the device behaves like a “normal” DLD device with a critical diameter  $\approx 6 \mu\text{m}$  ( $6 \mu\text{m}$  microspheres are in the mixed mode). When  $1 \text{ Vpp}$  @  $10 \text{ MHz}$  is applied to the device (red), the critical diameter decreases to  $\approx 4.5 \mu\text{m}$ . At  $2 \text{ Vpp}$  @  $10 \text{ MHz}$ , the critical diameter decreases further to around  $1.5 \mu\text{m}$ .

of the system. By tuning the frequency, different aspects of the particles are targeted for separation. As the frequency goes to zero (typically surface), conductivity dominates. As the frequency goes to infinity (typically bulk), permittivity dominates. Thus, for low frequencies, the surface of particles is probed whereas at high frequencies the bulk is probed. As a rule of thumb, positive DEP is the result at low frequencies and low medium conductivities. At high frequencies, the permittivity contrast between the particle and the medium dominates, and with the high permittivity of water, the resulting DEP is negative

$$\text{Re}[f_{\text{CM}}] = \frac{\tilde{\epsilon}_p - \tilde{\epsilon}_m}{\tilde{\epsilon}_p + 2\tilde{\epsilon}_m} \quad (4)$$

A thorough treatment of DEP can be found in Pethig’s textbook.<sup>[14]</sup>

### 2.3. Active Posts

As mentioned above, the major advantage of placing electrodes inside devices is that the maximum field gradient can be generated exactly where it has the greatest effect on the trajectories of the particles, using minimal applied voltage. While a similar effect could be achieved using a combination of 2D electrodes and 3D fluidic structures (for example, metal electrodes on a surface with PDMS structures on top), 3D electrodes have the major advantage that they provide a homogeneous electric field distribution over the complete depth of the device.<sup>[8a–d]</sup> This homogeneous distribution results in

forces that are invariant in the depth direction and the method is therefore also insensitive to buoyancy effects.

#### 2.4. Combining DLD and DEP Using Active Posts

In a DLD device, steric interactions between particles and posts cause particles to cross streamlines and to follow distinct trajectories through the device. As will be shown in Section 3, a DEP force can be created that, together with the steric interaction, can be sufficient to force a transition from the zigzag to the displacement mode. As described above, the DEP force is a function of the volume of the particle, the polarizabilities of the fluid and particles at the specific frequency, and the gradient of the electric field squared. In contrast to previous work by Beech et al.<sup>[6]</sup> with electrodeless DEP in DLD devices, placing the electrodes onto the surface of the posts allows high field gradients to be achieved over a large range of frequencies (0–10 MHz with our current function generator). The significant advantages of combining DEP and DLD in this way are that we can tune the critical size in a device (that otherwise only has one critical size) by simply turning the knobs on our function generator. As will be shown below, we can decrease the critical size by a factor of 24 and do so with a response time of seconds. This means that we can separate 4  $\mu\text{m}$  particles from 6  $\mu\text{m}$  particles, or, 250 nm particles from 500 nm in the same device. What's more, the gaps between the posts in the device are 10  $\mu\text{m}$ , making clogging negligible. We have run separations continuously for 10 h without clogging. Also, while the focus in this report is on size-based separation, the dependence of the DEP force on the polarizability of particles means that we also have a handle on separations by dielectric properties which can further aid us in identifying different types of cells or microorganisms as well as in differentiating cells in different states, e.g., in live/dead assays.

### 3. Results and Discussion

Figure 4 shows an example of the switching of modes (zigzag to displacement) in our device. In Figure 4A, 4.3  $\mu\text{m}$  microspheres, being smaller than the 6  $\mu\text{m}$  critical size in the device, move in the zigzag mode. Upon the application of 2 Vpp at 10 MHz (Figure 4B), the microspheres switch to the displacement mode. In Figure 4C, the trajectories of single microspheres are shown. In the bottom panel at 0 Vpp, the microsphere is in the zigzag mode. At 1.5 Vpp, the period in the zigzagging motion increases leading to greater displacement. At 2 Vpp, the microspheres are in full displacement mode. The change in the trajectories leads to the microspheres leaving the device at increasing outlet channel number as the applied voltage is increased. The position of each particle is established as shown in Figure 4E and the distributions plotted as shown in Figure 4D. In this way, the critical size in the device is tuned. Figure 3 shows outlet positions for seven different microparticle sizes and demonstrates how the critical size in the device changes as the applied voltage is increased from 0 to 2 V at 10 MHz.

We tested the response of the device to voltage scans at frequencies ranging from 1 Hz to 10 MHz. We find little to no separation below 100 kHz and also that at frequencies of 10 kHz and lower, at voltages above 3 Vpp, there is a tendency for microspheres to become trapped at the high field regions between the posts (see Figures S5 and S6 in the Supporting Information). We believe that this is likely due to positive dielectrophoresis or possibly AC electroosmosis although further experiments and simulations are needed to understand the mechanism in detail. We expect the optimal frequencies for tunable separation to depend on the types of particles being separated and frequency scans may well be the best approach to distinguish bioparticles with different polarizabilities. While tunable particle trapping by frequency scanning in these devices

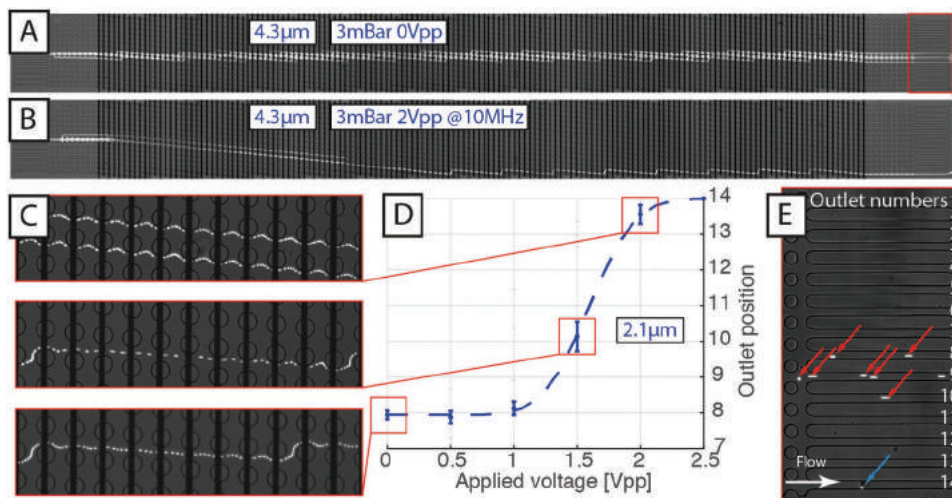


**Figure 4.** Typical separation results. A) 4.3  $\mu\text{m}$  microspheres are smaller than the native critical diameter ( $D_c \approx 6 \mu\text{m}$ ) in the device and therefore move in the zigzag mode. The image shows the entire separation area of the device. B) The same beads move in the displacement mode when 2 V @ 10 MHz is applied. Half way along the device, the microspheres hit the sidewall which leads to the zigzagging trajectory. C) Trajectories of individual 2.1  $\mu\text{m}$  microspheres as a function of applied voltage (10 MHz). D) Measured outlet channel numbers as a function of applied voltage for the same microspheres shown in (C). E) Analysis is performed by measuring the exit channel number for every microsphere. Red arrows show microspheres flowing out of the device and the blue arrow shows a stuck microsphere that is not counted.

may, in its own right, be interesting for a range of applications, here we have focused on studies of the behavior of the device at a single frequency. For the polystyrene microspheres we study here, all with the same polarizabilities, we find 10 MHz to be optimal for separation (see Figure S5 in the Supporting Information) and chose to keep the frequency fixed at 10 MHz and study the voltage dependence.

Figure 3 shows the effect of applied fields on the separation behavior of our device for a range of particle diameters. The green curve shows the device functioning without applied electric field. This is the baseline functionality of a DLD device. Microspheres with diameters below  $\approx 5 \mu\text{m}$  are in the zigzag mode and experience zero displacement. Microspheres with diameters above  $\approx 7 \mu\text{m}$  are fully displaced. Microspheres with diameters of  $\approx 6 \mu\text{m}$  are in the mixed mode and are only partially displaced. The critical size in this device, at zero applied field, can be approximated to  $\approx 6 \mu\text{m}$ . When 1 Vpp @ 10 MHz is applied to the device, the effective critical size in the device decreases to  $\approx 4.5 \mu\text{m}$  as shown by the red curve. At 2 Vpp, the critical size in the device decreases further to  $\approx 1.5 \mu\text{m}$ .

One obvious question here is how small we can make the critical size. Figure 5 shows the tuned separation of 0.25, 0.5, and 0.8  $\mu\text{m}$  microspheres at 10 MHz. At 0 Vpp, all microspheres are in the zigzag mode. At 3.5 Vpp, the 0.8  $\mu\text{m}$  microspheres move mostly in the displacement mode and become separated. At 5.25 Vpp, the 0.8  $\mu\text{m}$  microspheres are fully in the displacement mode, the 0.5  $\mu\text{m}$  are in the mixed mode, and the 0.25  $\mu\text{m}$  still in the zigzag mode. Here, the three microsphere populations are fully separated. This is particularly interesting because the device has only one critical size and if used in the traditional way, without applied fields, can usually only generate two fractions reliably. The mixed mode described above is difficult to predict and is most often seen as a factor that reduces device functionality and resolution. Here, we can reproducibly put particles in the mixed mode and create more than the expected 2 modes. At 7 Vpp, we are back to 2 fractions, one containing 0.25  $\mu\text{m}$  microspheres and the other containing 0.5  $\mu\text{m}$  and 0.8  $\mu\text{m}$  microspheres.

The trajectories (measured via outlet position) of eight microsphere populations as a function of applied voltage at 10 MHz are shown in Figure 6. The same data are split into two separate plots (Figure 6B,C) for clarity. As the voltage is increased, each microsphere population, in decreasing size order, makes the transition from the zigzag to the displacement modes via intermediate, mixed modes. In Figure 6A as mentioned above, the 7.81  $\mu\text{m}$  microspheres are displaced even at 0 Vpp applied voltage and 6.1  $\mu\text{m}$  are in the mixed mode half way between zigzag and displacement modes indicating that the geometry-based (zero-field)  $D_C$  in the device is  $\approx 6 \mu\text{m}$ . In Figure 6A,C, the 0.25  $\mu\text{m}$  particles enter the device with a slight offset (channel 9 rather than 8) which was due to a small clog in the inlet. The transitions are described well by error functions, shown fitted to the data. The error bars increase with decreasing particle size, consistent with diffusional broadening of the particle stream. Voltages can be found at which all particles are either displaced, nondisplaced, or somewhere in between and this can be changed with a switching time of seconds (see Section S8 in the Supporting Information). This is the fundamental principle of tuning using our method.

As the particles pass between the posts, there is a force balance between the viscous drag force and the DEP force that determines whether there is a transition from zigzag mode to displacement mode (Figure 7; Figure S7, Supporting Information). In Section S6 in the Supporting Information, we derive a scaling expression for the crossover voltage,  $V_C$

$$V_C^2 \propto \frac{R_C - R_{\text{particle}}}{R_{\text{particle}}^2} \frac{1}{\epsilon_m \text{Re}(f_{\text{CM}})} \frac{\Delta P w^4}{L} \quad (5)$$

Interestingly, the crossover voltage is independent of viscosity so that for a given device at a given applied pressure,  $\Delta P$ , the only important factors are the particle size,  $R_{\text{particle}}$ , in relation to the critical size,  $R_C$ , the dielectric properties of the medium and of the particle.

We verify the scaling relationship by two plots. First, we plot the crossover voltage versus the square root of the applied pressure

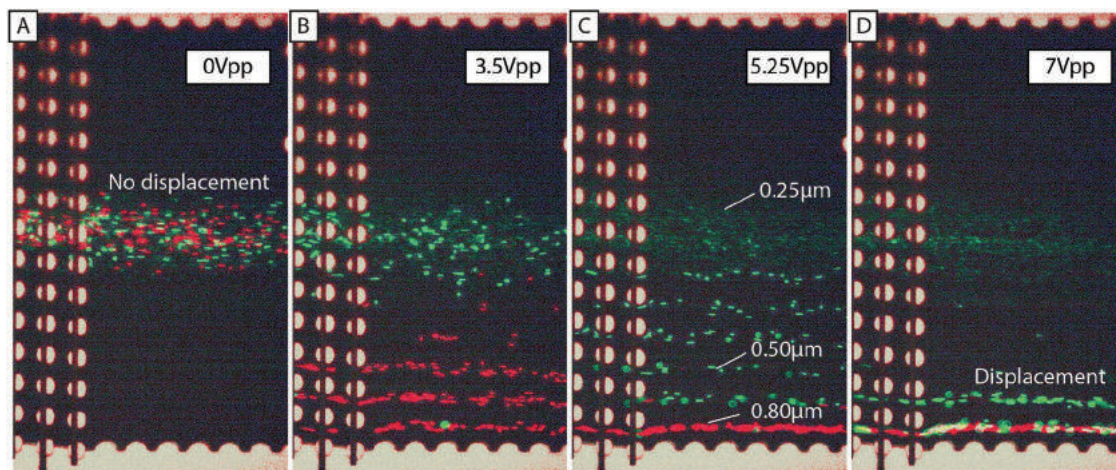


**Figure 5.** Tuned separation of 0.25, 0.5, and 0.8  $\mu\text{m}$  microspheres at 10 MHz and at A) 0 Vpp, B) 3.5 Vpp, C) 5.25 Vpp, and D) 7 Vpp. 0.25 and 0.5  $\mu\text{m}$  microspheres are green fluorescent and 0.8  $\mu\text{m}$  are blue fluorescent and were imaged with separate filter sets. The images were extracted from a movie, colorized and recombined to show all particles simultaneously. See the Supporting Information for the original movie.

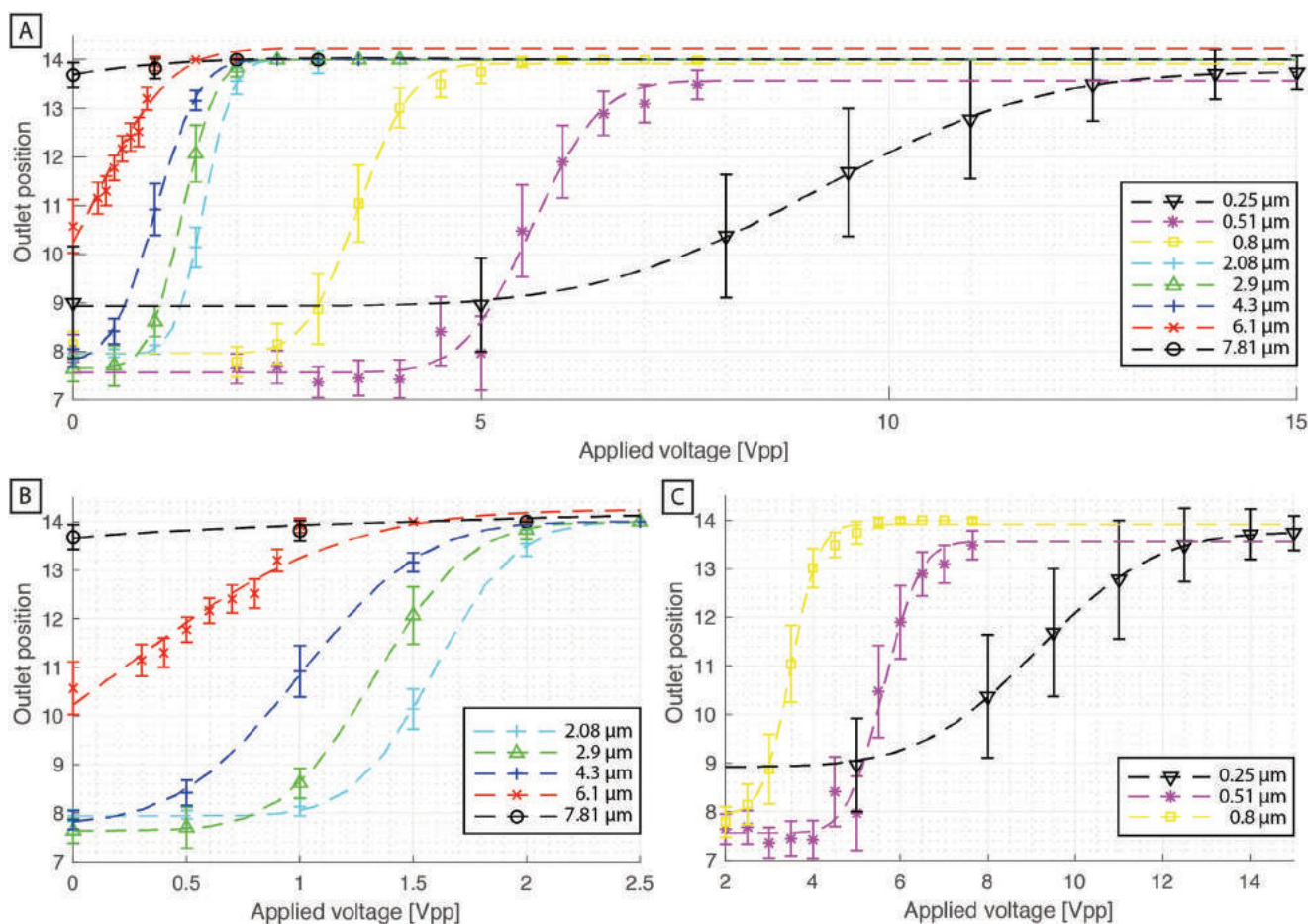


**Figure 6.** Outlet positions as a function of applied voltage (at 10 MHz) for A) 0.25, 0.51, 0.80, 2.08, 2.90, 4.30, 6.10, and 7.81  $\mu\text{m}$  microspheres. Particles exit at channel 8 if they experience no displacement and at 14 if they experience maximal displacement. The dashed lines show fitted error functions (see the Supporting Information for more information on fitting) except for the 7.81  $\mu\text{m}$  microspheres which is a spline. Error bars show one standard deviation. (B) and (C) show the same data with expanded x-axis for clarity.

in **Figure 8A**. Here, we use two criteria for the crossover. For each pressure, the voltage was tuned until the 4.3  $\mu\text{m}$  microspheres exited at the mean exit channel or at the threshold of maximum displacement.  $V_C$  is clearly linearly proportional to the square root

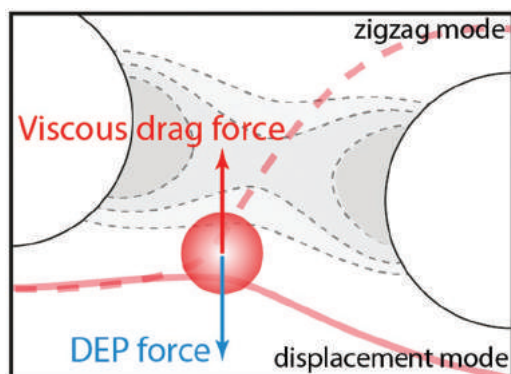


**Figure 7.** Illustration of the lateral components of the viscous drag force and DEP force. The viscous drag force acts to keep the particle in the zigzag mode whereas the DEP force pushes the particle into the displacement mode.

of the applied pressure in both cases. Second, we investigate the relationship between the crossover voltage and the particle size (**Figure 8B**). The crossover voltage is extracted from the fitted error functions in **Figure 6** as the voltage at which the particles exit at the mean exit channel, and the critical size is taken from the error function fit in **Figure 3** at zero applied voltage to be  $2R_C = 6.08 \mu\text{m}$ . Also, here we can demonstrate a linear relationship.  $V_C$  appears to be linearly proportional to  $((R_C - R_{\text{particle}})/R_{\text{particle}})^{0.5}$ , further supporting the validity of Equation (5).

The results of our simulations indicate that negative DEP is the force responsible for altering the trajectories of the particles. **Figure 9B** shows that there is good qualitative agreement between our experimental results and our simulations that take into account only forces due to drag, DEP, and steric interactions with the posts. Despite simplifications in the simulations (as explained above and in Section S4 in the Supporting Information) leading to an underestimation of the critical size, the transition from zigzag to displacement mode is captured faithfully. Interestingly, the mixed modes are not observed in the simulations. This is probably due to the fact that no anisotropy in the flow is present in the simulation. **Figure 9A** shows that greater negative DEP forces lead to greater displacements.

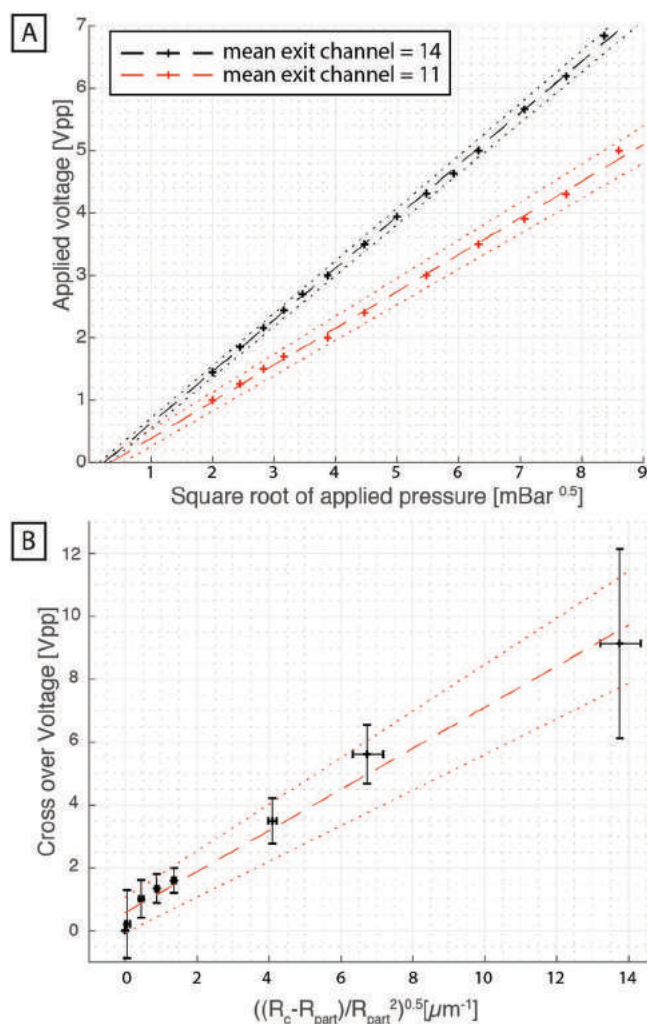


**Figure 8.** Crossover voltages as a function of applied pressure and particle size. A) Red crosses show crossover voltages (mean exit channel number is 11) for 4.30  $\mu\text{m}$  microspheres as a function of the square root of the applied pressure. The black crosses show the voltage at which maximum displacement (mean exit channel number is 14) is first reached.  $R$ -square of the fit is 0.9979. B) Crossover voltage as a function of  $((R_c - R_{\text{part}})/R_{\text{part}})^{0.5}$ . Here, the  $R$ -square of the fit is 0.9826. In all cases, the error bars show one standard deviation and the lines show a linear fit with 95% confidence intervals.

The dynamic range of a DLD device can be defined as the ratio of the largest to smallest critical diameters that can be achieved.<sup>[15]</sup> Increasing this range is often done using so-called chirped arrays, i.e., multiple DLD array in sequence. However, as Davis discusses in his thesis,<sup>[9]</sup> the maximum particle size that can be handled is limited to the smallest gap size in the device, which ultimately limits dynamic range to between 3 and 5. Cascaded devices have channels that remove large particles between the cascaded arrays and in these dynamic ranges of 20 can be achieved, but at the cost of increased complexity of both design and performing separations.

Because our device has only one critical size ( $D_C \approx 6 \mu\text{m}$ ), it has a dynamic range of one, when not using the active post capabilities. However, since we are able to displace

0.25  $\mu\text{m}$  particles in our device by applying electric fields, we have increased the dynamic range to  $\approx 24$ . By combining our active post approach with the chirped and cascaded device approach, we believe we could achieve dynamic ranges greater than 100.

Lastly, we can also consider the lower limit for  $D_C$  as the applied voltage is increased. With our current setup, we were unable to apply higher voltages at 10 MHz than those required to displace 250 nm particles. However, at frequencies below 1 MHz, we were able to test the maximum voltage that the device could sustain. At  $\approx 40$  Vpp, rapid bubble formation was observed. The threshold for bubble formation was observed to decrease with increasing ionic strength ( $\approx 30$  Vpp for 1500  $\text{mS m}^{-1}$  KCl compared to  $\approx 40$  Vpp for milliQ at  $\approx 0$   $\text{mS m}^{-1}$ ). Bubbles also formed at lower voltages for lower frequencies ( $\approx 30$  Vpp @ 1 KHz compared to  $\approx 40$  Vpp @ 1 MHz). Higher flow rates also decreased the threshold for bubble formation. At 25  $\text{mS m}^{-1}$  KCl, 40 Vpp @ 5 MHz bubbles formed at 77 mBar but not at 500 mBar. Lastly, cooling the device with ice also decreased the threshold slightly. Taken together, these results indicate that bubble formation is probably due to joule heating where the power density is proportional to the electric field squared and to the conductivity. Further studies are required to ascertain exactly how much heating is occurring under the conditions used for separation but we can at least conclude that we are working far below the limits for excessive heating and that we have strategies (such as cooling) that could be used where heating could be a problem, such as for bioseparations requiring high ionic strengths. We also observed some hysteresis after boiling, with the threshold decreasing after an initial boiling event. This, we believe, could be due to damage to the device although full breakdown of the electrodes and SU8 structures in the device occurred first at voltages well above 100 Vpp.

## 4. Conclusion

We have successfully demonstrated proof of principle of a DLD device combined with electrodes directly integrated onto the posts. The short interelectrode distances allow us to reach high electric field strengths, on the order of nominally 1  $\text{MV m}^{-1}$ , at high frequencies with small enough voltages to ensure simple and safe operation.

We have shown that we can change the critical size in our device from  $D_C \approx 6 \mu\text{m}$  to 250 nm, a decrease by a factor of 24, which constitutes an increase in dynamic range by the same factor. We predict that at higher applied voltages, we will be able to decrease the critical size further although heating could be a problem at excessive applied voltages. Alternatively, devices with a smaller critical size of  $D_C = 2 \mu\text{m}$  would be within the capabilities of the fabrication method we have used here. Applying electric fields to these devices and decreasing the critical size by the same factor as shown here (24) would allow us to separate particles in the sub 100 nm diameter range. Switching times in our device depend on flow rates, but at the conditions presented here, they are in the range of several seconds. This means that we can immediately visualize the response to a change in voltage and tune separations in real

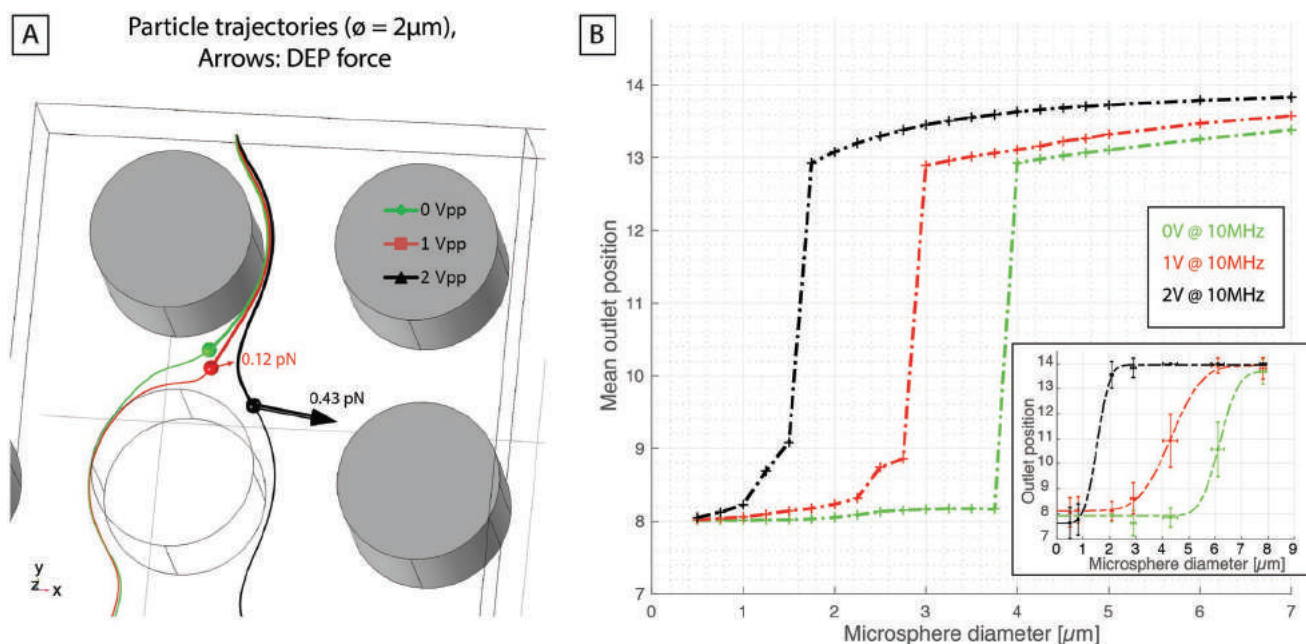


**Figure 9.** Numerical simulations performed in COMSOL Multiphysics 5.3a including viscous drag and DEP forces only capture the behavior of our devices. Full details of simulations can be found in Section S4 in the Supporting Information. A) Microspheres of  $2\mu\text{m}$  diameter at 0, 1, and 2 Vpp (10 MHz) applied field. At 2 Vpp, the DEP force (the arrows show the direction and magnitude of the DEP force) is sufficient to push the microspheres into the displacement mode. B) Simulations of many microsphere diameters and three applied voltages at 10 MHz. The inset shows experimental results under the same conditions (repeated from Figure 3 for ease of comparison).

time. At high flow rates or applied voltages, the switching times will be shorter. To summarize, we change what is essentially a bimodal separation technique into a tunable multimodal separation tool. Further studies will focus on the application of the method to biological particle systems.

## 5. Experimental Section

**Device Fabrication:** The detailed fabrication process is described in Figure S1 in the Supporting Information. A metal layer (Ti/Pt/Ti 20 nm/200 nm/20 nm) was first sputtered onto a plane glass substrate and patterned by ion beam etching. The metal lines were then covered with an insulating  $\text{SiO}_2$  layer (300 nm) and vias to connect the electrodes were etched by reactive ion etching. To create the active electrode structures, SU-8 pillars were patterned (15  $\mu\text{m}$  thick) and were subsequently coated by metal sputtering (Ti/Pt 20 nm/200 nm). The metal deposited on top of the pillars and on the planar substrate was removed by directional ion beam etching. This etching process preserved the metal-coated side walls of the electrodes.<sup>[8]</sup>

A second SU-8 lithography step was used to define the fluidic channels and all other nonelectrically active device features. Channels were sealed with an  $\approx 4\text{ mm}$  thick PDMS slab using oxygen plasma and APTES.<sup>[16]</sup> Before sealing, holes were punched through the slab for fluidic access. After sealing, silicone tubes were glued to the PDMS to function as fluid reservoirs and for interfacing with a pressure control unit. Wires were soldered to the device for electrical connection. The final device is shown in Figure 2B. Further device details, such as the measured dimensions of the final device, can be found in Figure S2 in the Supporting Information.

**Experimental Setup, Method, and Materials:** Flow in the devices was generated by applying overpressure in the range of 2–75 mBar to the device inlets using an MFCS-4C pressure controller (Fluigent, Paris, France). Outlet reservoirs were kept at ambient pressure. A function generator (15 MHz function/arbitrary waveform generator,

model 33120A, Hewlett Packard, Palo Alto, CA, USA) was used for the application of AC signals. The applied voltage signal was monitored with an oscilloscope (Hewlett Packard 54603B 60 MHz) with a  $1\times/10\times$  probe (Kenwood PC-54, 600 Vpp). All images were captured through a microscope (Nikon Eclipse TE2000-U, Nikon Corporation, Tokyo, Japan), with an Andor Neo CMOS camera (Andor Technology, Belfast, Northern Ireland) using NIS Element software (NIS Element Advanced Research v4.51, Nikon). The conductivities of the media and the suspensions used in all experiments were measured using a B-771 LAQUAtwin Compact Conductivity Meter (Horiba Instruments).

$1.7 \times 10^{-3}\text{ M}$  KCl with 0.1% Pluronic F127 (conductivity measured at  $25\text{ mS m}^{-1}$ ) was used as a suspending medium for latex beads of varied diameters ( $0.25 \pm 0.01$ ,  $0.51 \pm 0.03$ , and  $0.8 \pm 0.02\mu\text{m}$  from Duke Scientific;  $2.08 \pm 0.06$ ,  $2.9 \pm 0.09$ ,  $4.3 \pm 0.27$ , and  $6.1 \pm 0.24\mu\text{m}$  from PolySciences;  $7.81 \pm 0.11\mu\text{m}$  from Micro Particles GmbH). The bead suspensions were driven through the device using a pressure difference in the range of 2–75 mBar. Frequencies ranging between 1 Hz and 10 MHz and peak to peak voltages ranging between 0.5 and 15 Vpp were applied to the devices and the trajectories (exit positions) of the microspheres were measured.

**Particle Counting and Analysis:** The separation of particles was determined by manual counting at the end of the DLD array. The process is described in detail in Section S3 in the Supporting Information and in Figure 4. In short, the number of particles exiting the device through each of the 14 exit channels was established by manual inspection of recorded movies for each of the experimental conditions (varied voltage, frequency, and pressure) and for each of the particle sizes.

**Simulations:** In order to gain insight into the distribution of the electric field inside the device and to aid in the understanding of how devices work, numerical simulations were performed in COMSOL Multiphysics 5.3a. In brief, trajectories of particles of different sizes were simulated moving through a device under conditions similar to those in the experiments. COMSOL's "laminar flow" module and "electric current" module were used to simulate both fluid flow velocity and electric fields, and the trajectories of particles of different sizes moving through these fields were then calculated using the "particle tracing for fluid flow" module. Full details are given in Section S4 in the Supporting Information, and results can be seen in Figure 9 above.

## Supporting Information

Supporting Information is available from the Wiley Online Library or from the author.

## Acknowledgements

The parts of this work carried out at NanoLund were supported by the BeyondSeq consortium (EU Horizon2020 project 634890), the evFOUNDRY consortium (EU Horizon2020 project 801367), and the Swedish Research Council (grant no. 2016-05739), and those carried out at EPFL by the Swiss National Science Foundation (205321\_179086). The authors are thankful for support from the Centre for MicroNanotechnology at EPFL, where the chips were fabricated.

## Conflict of Interest

The authors declare no conflict of interest.

## Keywords

3D electrodes, deterministic lateral displacement, dielectrophoresis, particle sorting, tunable separation

Received: April 23, 2019

Revised: June 7, 2019

Published online:

[1] L. R. Huang, E. C. Cox, R. H. Austin, J. C. Sturm, *Science* **2004**, *304*, 987.

[2] Occasionally, when we do not need to be specific about whether we refer to the radius or the diameter, we use the term critical size instead.

- [3] J. P. Beech, J. O. Tegenfeldt, *Lab Chip* **2008**, *8*, 657.
- [4] K. K. Zeming, N. V. Thakor, Y. Zhang, C. H. Chen, *Lab Chip* **2016**, *16*, 75.
- [5] K. K. Zeming, T. Salafi, S. Shikha, Y. Zhang, *Nat. Commun.* **2018**, *9*, 1254.
- [6] J. P. Beech, P. Jonsson, J. O. Tegenfeldt, *Lab Chip* **2009**, *9*, 2698.
- [7] C. F. Chou, J. O. Tegenfeldt, O. Bakajin, S. S. Chan, E. C. Cox, N. Darnton, T. Duke, R. H. Austin, *Biophys. J.* **2002**, *83*, 2170.
- [8] a) E. Rollo, E. Tenaglia, R. Genoblet, E. Bianchi, A. Harari, G. Coukos, C. Guiducci, *Biosens. Bioelectron.* **2017**, *94*, 193; b) K. Keim, M. Z. Rashed, S. C. Kilchenmann, A. Delattre, A. F. Gonçalves, P. Éry, C. Guiducci, *Electrophoresis* **2019**, <https://doi.org/10.1002/elps.201900097>; c) L. S. Wang, L. Flanagan, A. P. Lee, *J. Microelectromech. Syst.* **2007**, *16*, 454; d) S. C. Kilchenmann, E. Rollo, P. Maoddi, C. Guiducci, *J. Microelectromech. Syst.* **2016**, *25*, 425.
- [9] J. A. Davis, *Ph.D. Thesis*, Princeton University **2008**.
- [10] T. Kulrattanakarak, R. G. M. van der Sman, Y. S. Lubbersen, C. G. P. H. Schroen, H. T. M. Pham, P. M. Sarro, R. M. Boom, *J. Colloid Interface Sci.* **2011**, *354*, 7.
- [11] Z. Zhang, E. Henry, G. Gompfer, D. A. Fedosov, *J. Chem. Phys.* **2015**, *143*, 243145.
- [12] R. Vernekar, T. Kruger, K. Loutharback, K. Morton, D. W. Inglis, *Lab Chip* **2017**, *17*, 3318.
- [13] S. C. Kim, B. H. Wunsch, H. Hu, J. T. Smith, R. H. Austin, G. Stolovitzky, *Proc. Natl. Acad. Sci. USA* **2017**, *114*, E5034.
- [14] R. R. Pethig, *Dielectrophoresis: Theory, Methodology and Biological Applications*, 1st ed., Wiley, Chichester, West Sussex, UK **2017**, p. 448.
- [15] J. A. Davis, D. W. Inglis, K. J. Morton, D. A. Lawrence, L. R. Huang, S. Y. Chou, J. C. Sturm, R. H. Austin, *Proc. Natl. Acad. Sci. USA* **2006**, *103*, 14779.
- [16] Y. F. Ren, S. H. Huang, S. Mosser, M. O. Heuschkel, A. Bertsch, P. C. Fraering, J. J. Chen, P. Renaud, *Micromachines* **2015**, *6*, 1923.



## Supporting Information

for *Adv. Mater. Technol.*, DOI: 10.1002/admt.201900339

Active Posts in Deterministic Lateral Displacement Devices

*Jason P. Beech,\* Kevin Keim, Bao Dang Ho, Carlotta Guiducci, and Jonas O. Tegenfeldt\**

Copyright WILEY-VCH Verlag GmbH & Co. KGaA, 69469 Weinheim, Germany, 2019.

## Supporting Information

### Title Active Posts in Deterministic Lateral Displacement Devices

Jason P. Beech\*, Kevin Keim, Bao Dang Ho, Carlotta Guiducci\*, Jonas O. Tegenfeldt\*

## 1. Device Fabrication

Fabrication was performed following the protocol depicted in Figure S 1.

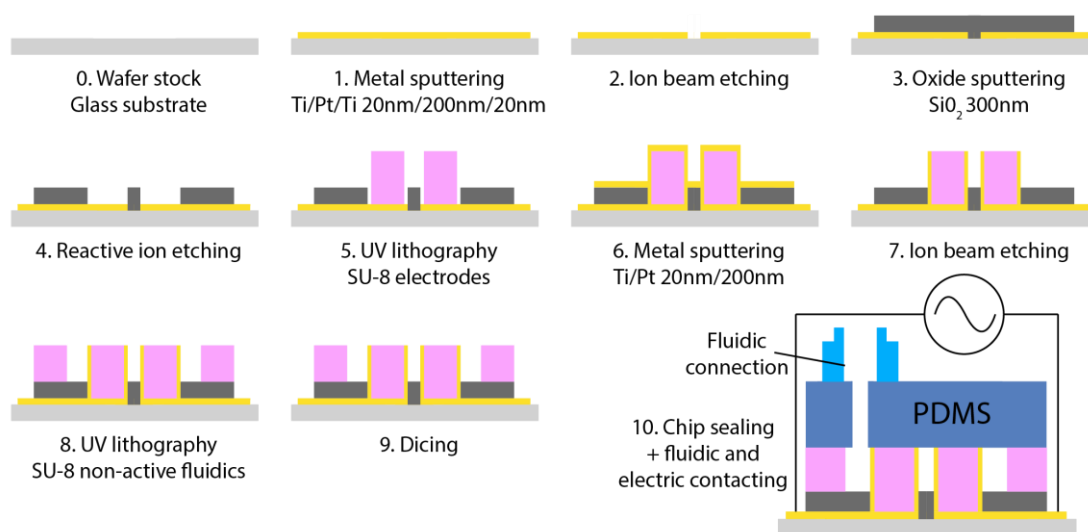


Figure S 1. The process flow for the fabrication of devices containing metal-coated, three-dimensional electrode structures with insulated connection lines. These three-dimensional electrodes constitute the pillars that make up a DLD separation array.

## 2. Device Layout

The device is designed with the layout and dimensions shown in Figure S 2. Using the fabrication method described above both the active electrode structures inside the DLD array (defined in step 5 in Figure S 1) and the non-active features, such as the three inlets for

particle focusing and the outlet for collection and counting of particles (defined in step 8 in Figure S 1) are achieved.

While the device was designed to have a  $D_C$  of  $5.56\mu\text{m}$  (based on  $G = 12\mu\text{m}$  and  $N = 10$ , see Equation (1) in the main text) the dimensions of the actual devices differed slightly from the designed parameters giving a somewhat smaller  $D_C$ . Figure S 2D and E show how the attained gaps in our final devices were determined to be  $G = 11.10 \pm 0.14\mu\text{m}$  giving a  $D_C = 5.15 \pm 0.06\mu\text{m}$ . The depth of the device is  $13\mu\text{m}$  as determined by direct measurement using SEM.

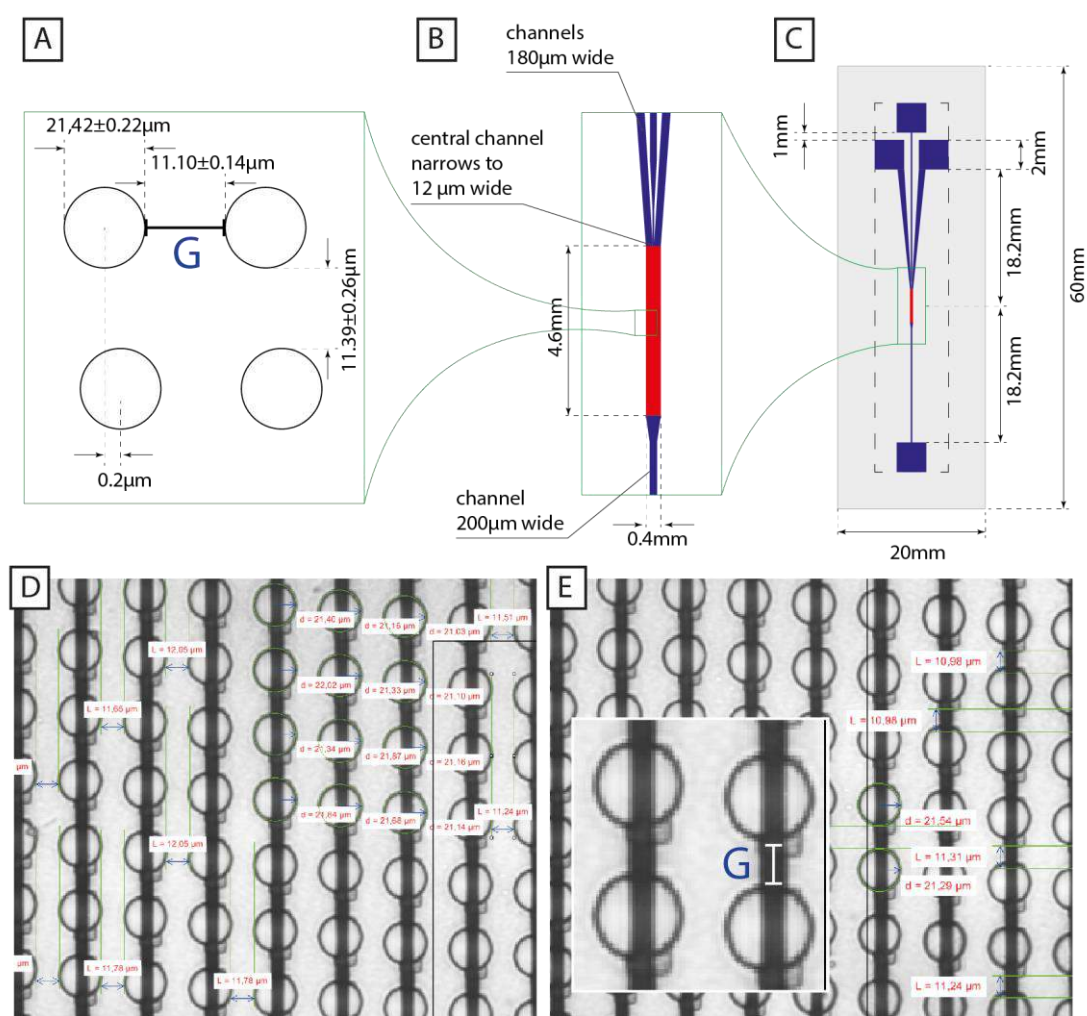


Figure S 2. Designed and measured device and DLD array dimensions. A) Measured dimensions of fabricated DLD arrays. B) Dimensions of DLD array, inlet and outlet channels. C) Dimensions of the final, diced device with the inlet and outlet reservoir-connection areas shown. D) and E) Measurements are performed using NIS elements, 20x objective (NA 0.5, 2.0 mm WD) from Nikon.

### 3. Particle counting and Analysis

In order to establish the trajectories of particles (and determine the performance of the separations) the position of every particle was determined as they left the separation array in the device. The device was designed with 14 parallel channels at the outlet in which to perform this measurement, see Figure S 3. To ensure an accurate count of particles and to minimize false counts the measurement itself was performed by manual inspection of the recorded movies. For each experimental condition (1 voltage, 1 frequency and 1 microparticle size) several hundred events were measured.

Individual 250nm microspheres could not be imaged separately. Here the fluorescence intensity profile across the outlet of the device was determined and the particle distribution related linearly to the intensity.

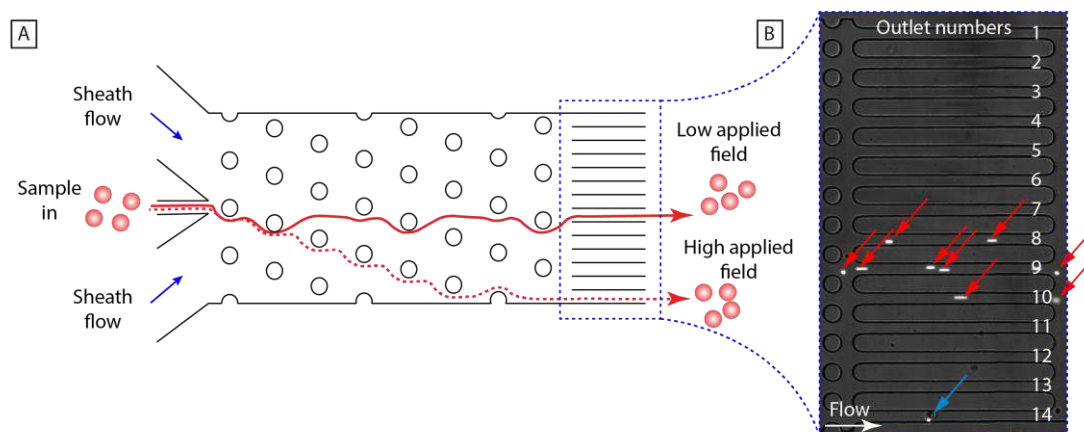


Figure S 3. The device has 14 outlet channels where the particles are counted. Outlet #8 corresponds to no displacement in the DLD device. Outlet #14 corresponds to maximum displacement.

### 4. Simulations

Numerical simulations were carried out using COMSOL Multiphysics<sup>®</sup> 5.3a to gain more insights into experimental results. A subset of the device, an array of 20x4 posts, was generated in 3D with the same geometry (measured) as that of our final device (Figure S 4). In the figure, the pillars are in grey color with red/blue walls representing the biased voltage

terminals and the fluid is left transparent for visibility. Exemplified trajectories of four 6  $\mu\text{m}$  particles are also shown.

Our goal is to model trajectories of particles of different sizes being transported in our device under certain values of applied pressure and applied voltage. Firstly, fluidic velocity field due to the applied pressure and electric field due to the applied voltage were solved, using COMSOL's "*Laminar flow*" module and "*Electric current*" module, respectively. Based on the values of the fields, Stokes' drag force and dielectrophoretic force acting on the particles can be computed. The values of the velocity field and the electric field were taken at the centers of the particles and the perturbation of the fields due to the presence of the particles was neglected. In addition to the drag force and the dielectrophoretic force, a wall steric force was applied when the particles were in contact with the walls. To track the distances between the particles and the walls, the "*Wall distance*" module was used. Finally, after the drag force, the dielectrophoretic force, and the wall repulsive force were resolved, the trajectories of the particles could be computed using the "*Particle tracing for fluid flow*" module. Differential equations and boundary conditions corresponding to the modules employed in the simulation are listed in Table S1, the variable/parameter names and values are listed in Table S2, and some representative results are shown in Figure S 4B to E.

There are some technical "tricks" we used to ensure accuracy of the results and reasonable computational time. First of all, since the model is a periodic subset of the device, periodic boundary conditions were applied at the four vertical walls of the model, for "*Laminar flow*", "*Electric current*", and "*Wall distance*" module. Furthermore, for "*Laminar flow*" module, a small lateral pressure ( $\sim 0.6\%$  of the pressure at the inlet) was applied between the two vertical walls on the right and the left-hand side to ensure an overall straight flow, as in the whole device. Without this lateral pressure, the simulated flow field would be tilted towards the right-hand side due to the orientation of the pillars. Second of all, the computing time can be too long for the "*Laminar flow*" module and the "*Wall distance*"

module at fine mesh size, due to large number of mesh elements. To circumvent this problem, we notice that our 20x4 periodic geometry can be partition further into four 10x2 geometries, also periodic. The “*Laminar flow*” module and the “*Wall distance*” module can be solved in one of these four smaller periodic geometries, and the solutions can be then copied to the three remaining ones, ready for subsequent computation of particle trajectories.

To simulate particle trajectories, for each particle size and each value of the applied voltage (0, 1, and 2 V<sub>pp</sub>), four particles were placed evenly at four different positions near the first gap at the inlet of the 20x4 geometry (Figure S 3A). The particles were then transported along the geometry, in the y-direction, mainly due to the Stokes’ drag force. The dielectrophoretic (DEP) force, on the other hand, acts largely in the x-direction. For polystyrene beads under the conditions employed in this work (Table S2), the DEP force pushes particles away from the strong field locations (negative DEP) and tends to increase the displacing tendency of the particles (Figure S 4C and E). To quantify the degree of displacement of the particles, their displacing angles were calculated based on their initial and final positions and plotted as a function of their diameters and the applied voltage (**Error! Reference source not found.**B in the main text). Note that the displacement angles have been translated into mean outlet positions to facilitate comparison with the experimental data.

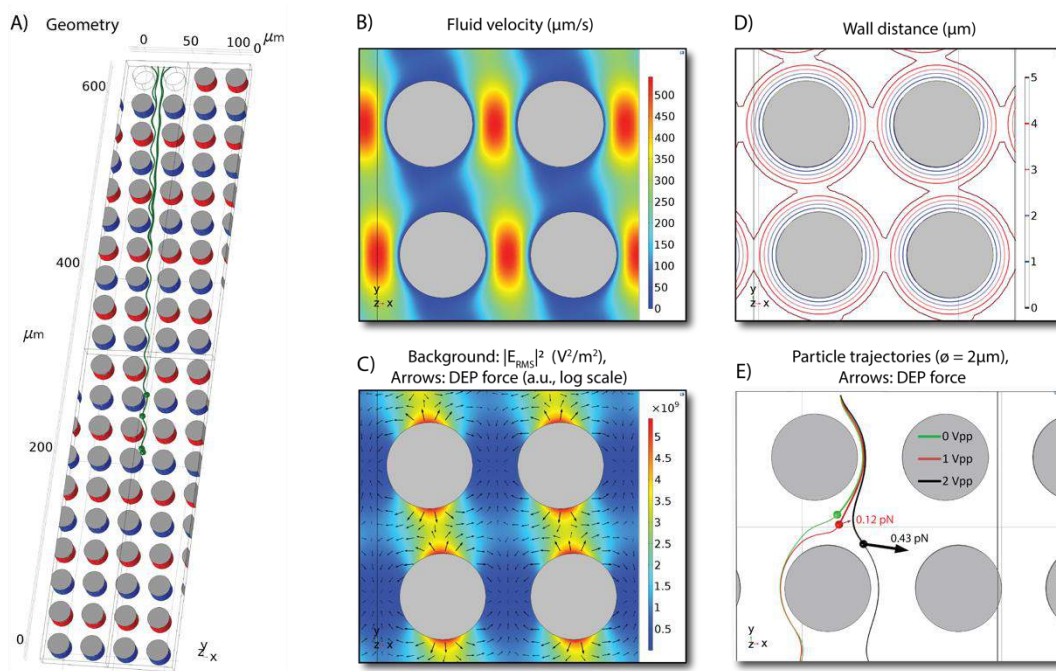


Figure S 4. Numerical simulation using COMSOL Multiphysics 5.3a. (A) Pillar array (20x4). (B) Fluid velocity (C) Colormap shows the square of the electric field and the arrows, the magnitude and direction of the DEP force (for a particle experiencing negative DEP) (D) Contour map of wall distance (1 μm steps). (E) Microspheres of 2 μm diameter at 0, 1 and 2 Vpp (10 MHz) applied field. At 2 Vpp the DEP force (the arrows show the direction and magnitude of the force) is sufficient to push the microspheres into the displacement mode.

Table S1. The differential equations and the boundary conditions of the modules used in the simulations.

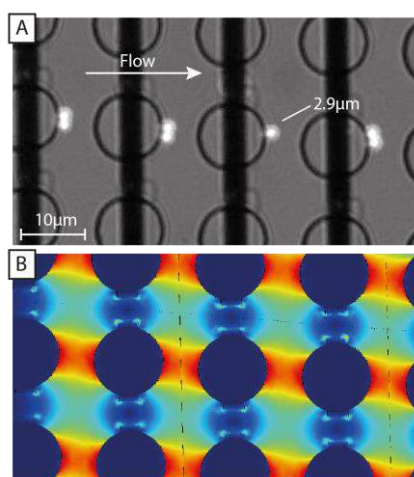
Module	Differential equations/Boundary conditions	Meaning
Stokes flow	$0 = \nabla \cdot [-p\mathbf{I} + \eta(\nabla\mathbf{u} + (\nabla\mathbf{u})^T)] + \mathbf{F}$	Force balance, left hand side: inertial term neglected, right hand side: surface forces and body forces add up to zero.
	$\rho\nabla \cdot \mathbf{u} = 0$	Mass continuity equation for incompressible flow
	$\mathbf{u} = 0 \text{ }  _{walls}$	No-slip boundary condition at walls in pressure driven flow
	$p \text{ }  _{inlet} = p_0, p \text{ }  _{outlet} = 0$	Pressure at inlet and outlet of the model
Electric current	$\nabla \cdot \mathbf{J} = 0$	Continuity equation for electric current
	$\mathbf{J} = (\sigma + i\omega\varepsilon_0\varepsilon_r)\mathbf{E}$	Ohm's law in frequency domain
	$\mathbf{E} = -\nabla V$	Definition of electric potential
	$V \text{ }  _{odd \text{ rows}} = V_0, V \text{ }  _{even \text{ rows}} = 0$	AC voltage, magnitude of $V_0$ , is applied between every two consecutive rows
Wall distance	$ \nabla D_w  = 1$	The norm of the gradient of wall distance is unity.
	$D_w \text{ }  _{wall} = 0$	The wall distance is zero at the walls.
Particle tracing for fluid flow	$\frac{d}{dt}(m_p\mathbf{v}) = \mathbf{F}_t$	Newton's second law of motion
	$\mathbf{F}_d = \frac{1}{r_p}m_p(\mathbf{u} - \mathbf{v})$	Drag force, Stokes form used for laminar flow
	$\tau_p = \frac{\rho_p d_p^2}{18\eta}$	Particle velocity response time for spherical particles in a laminar flow
	$\mathbf{F}_w = F_{w0} \times step(D_w - r_p) \times (-\mathbf{D}_{dir})$	Wall steric repulsive force
	$\mathbf{F}_{DEP} = 2\pi r_p^3 \varepsilon_m Re\{f_{CM}\} \nabla  \mathbf{E}_{rms} ^2$	Dielectrophoretic force
	$f_{CM} = \frac{\tilde{\varepsilon}_p - \tilde{\varepsilon}_m}{\tilde{\varepsilon}_p + 2\tilde{\varepsilon}_m}$	The Clausius-Mosotti factor
	$\tilde{\varepsilon}_m = \varepsilon_m - j\frac{\sigma_m}{\omega}$	Complex permittivity of medium in frequency domain
	$\tilde{\varepsilon}_p = \varepsilon_p - j\frac{\sigma_p}{\omega}$	Complex permittivity of particle in frequency domain
	$\sigma_p = \frac{2K}{r_p}$	Conductivity of polystyrene particle can be attributed to its surface conductance, the bulk conductivity can be neglected.

Table S2. The variables and parameters used in the simulations.

Notation	Value	Meaning	Notation	Value	Meaning
$\mathbf{D}_{dir}$		Direction toward the nearest wall (unit vector)	$p$		Pressure
$D_w$		Distance from the center of a particle to the nearest wall.	$p_0$	10.075 Pa	Pressure at the inlet of the 10x2 geometry (corresponding to an applied pressure of 3 mBar at the inlet of the device)
$d_p$	0.5 – 7 $\mu\text{m}$	Particle diameter	$p_{lateral}$	0.058 Pa	Pressure between the two vertical walls on the side to ensure an overall straight flow (10x2 geometry)
$\mathbf{E}, \mathbf{E}_{rms}$		Electric field, electric field (root mean square)	$Re\{\}$		The real part of ...
$\mathbf{F}$		Body force	$r_p$	0.25 – 3.5 $\mu\text{m}$	Particle radius
$f$	10 MHz	Frequency of electric field	$step()$		Step function, jumping from 1 at the wall down to 0 at 0.02 $\mu\text{m}$ from the wall.
$\mathbf{F}_t$		Total force acting on particle	$t$		Time
$\mathbf{F}_d$		Stokes' drag force acting on particle	$\mathbf{u}, \mathbf{v}$		Velocity of fluid and of particle, respectively
$\mathbf{F}_{DEP}$		Dielectrophoretic force acting on particle	$V$		Electric potential
$\mathbf{F}_w$		Steric wall force acting on particle	$\nabla$		Del operator
$F_{w0}$	20 pN	Maximum wall force. The wall force reach this value when a particle is in contact with the wall.	$\varepsilon_m, \varepsilon_p$		Permittivity of medium and of particle
$f_{CM}$		The Clausius-Mosotti factor	$\eta$		Dynamic viscosity of fluid
$G$	11.1 $\mu\text{m}$	Gap between two pillars of the DLD array	$\rho, \rho_p$		Mass density of fluid and of particle
$\mathbf{I}$		Identity matrix	$\sigma_m, \sigma_p$		Conductivity of medium and of particle
$j$		The imaginary unit ( $j = \sqrt{-1}$ )	$\tau_p$		Particle velocity response time in Stokes flow
$\mathbf{J}$		Current density	$\omega$		Angular frequency
$K$	2 nS	Surface conductance			
$m_p$		Mass of particle			
$N$	10	Period of the DLD array			

## 5. Frequency response

We measured the outlet distributions as a function of applied voltage for 4.3  $\mu\text{m}$ , 2.9  $\mu\text{m}$  and 2.1  $\mu\text{m}$  polystyrene microspheres at frequencies between 1 Hz and  $10^7$  Hz. There are several results that are worth pointing out. The transitions between zigzag and displacement modes are most well defined at  $10^6$  and  $10^7$  Hz. We chose therefore to study smaller microspheres at  $10^7$  Hz (see results in the main article). At 1 Hz and 10 Hz there is no change in trajectories. At 100 Hz and 1000 Hz and 3 V<sub>pp</sub> to 4 V<sub>pp</sub> applied voltage, particles become trapped. Figure S 5 shows 2.9  $\mu\text{m}$  particles trapped at high-field regions implying that it could be due to positive DEP. However, polystyrene microspheres are not expected to experience positive DEP under these conditions. Further studies are needed to fully explain this trapping but AC electroosmosis could be involved. We observed a tendency for 2.9  $\mu\text{m}$  microspheres to become negatively displaced at lower frequencies, see blue lines in Figure S 6. We believe that this “negative” displacement is related to the same mechanism as the trapping mentioned above. Again, further studies are required to understand this mechanism. For the work in this paper we chose to work at 10 MHz, far from the trapping regime.



*Figure S 5. Particles can become trapped at high-field regions. (A) At 1000 Hz and 4 V<sub>pp</sub> applied voltage (3 mBar applied pressure) 2.9  $\mu\text{m}$  microspheres become trapped. (B) By comparison with simulations of the electric field we can confirm that trapping occurs at high field regions. Because the microspheres are moving from left to right, they enter trapping regions preferentially on the right-hand side of each post.*

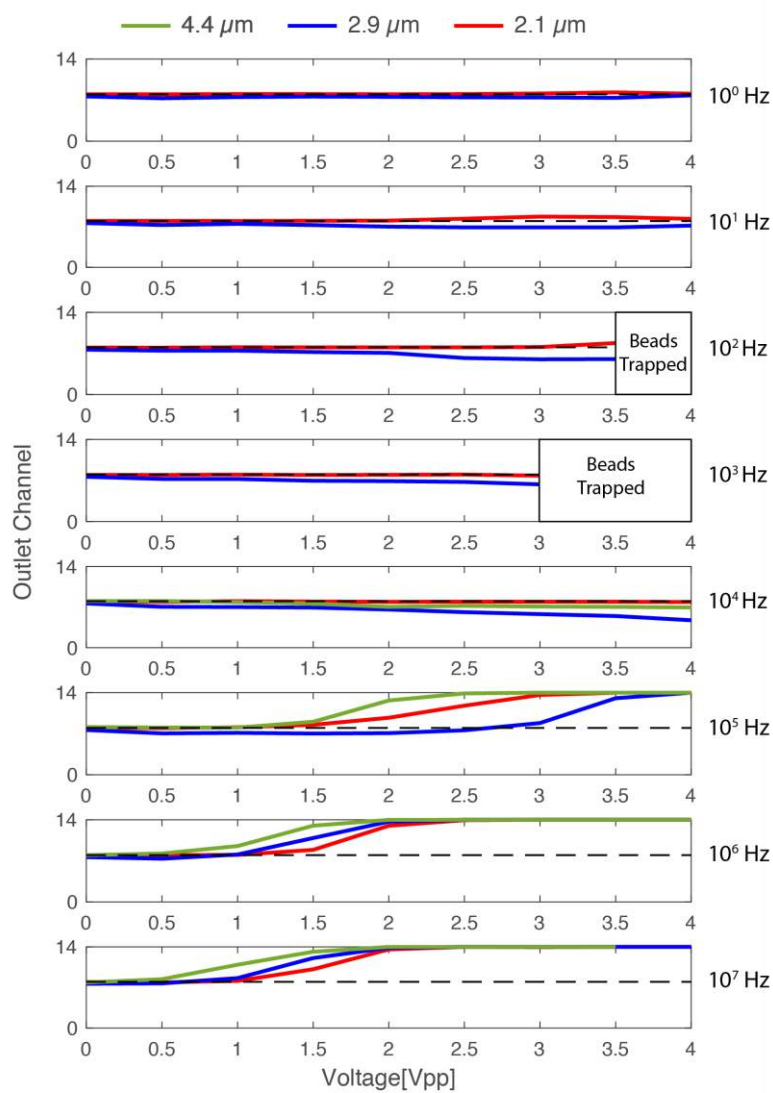


Figure S 6. The outlet positions as a function of applied voltage for three bead sizes at frequencies ranging from 1 Hz to 10 MHz.

## 6. Theoretical derivation of relationship between crossover voltage, particle radius and applied pressure.

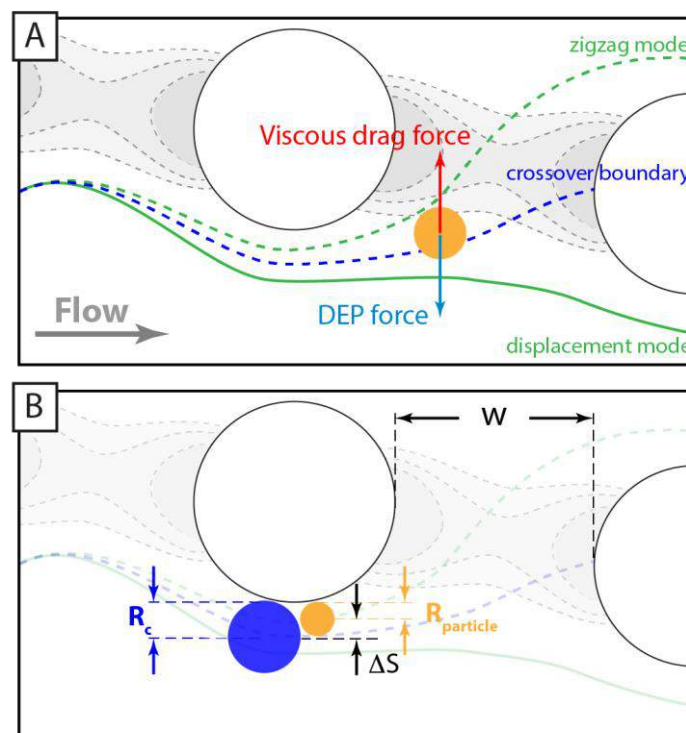


Figure S 7. Definitions for theory derivation. (A) A particle moving through a DLD device experiences viscous drag forces that keep it moving with the fluid flow direction if its radius  $R_{particle}$  is smaller than the critical radius  $R_c$ . If  $R_{particle}$  is greater than  $R_c$ , then the particle will move in the displacement mode. Alternatively, a particle with  $R_{particle}$  less than  $R_c$  can be pushed into the displacement mode by an additional force. Here the force is a negative dielectrophoretic force. (B) To first approximation, a particle needs to be pushed a distance  $\Delta S$  in order to transition from zigzag to displacement modes.

We define the cross-over voltage,  $V_C$ , as the voltage at which a given particle transitions from zigzag mode to displacement mode. To elucidate the underlying mechanisms, we here derive scaling relationships between  $V_C$  and relevant experimental parameters.

As illustrated in Figure S 7, to first approximation, a particle that is smaller than the critical radius needs to be pushed a distance  $\Delta S$  in order to make the transition from zigzag to displacement modes:

Equation S1

$$\Delta S = R_c - R_{particle}$$

The distance the particle is pushed by the DEP force is also given by the product of velocity due to the DEP force,  $v_{DEP}$ , and the time that the force acts,  $t_{DEP}$ :

Equation S2

$$\Delta S = v_{DEP} \cdot t_{DEP}$$

The time  $t_{DEP}$  is in turn given by the distance  $w$  (see Figure S 7) divided by the flow velocity  $v_{flow}$ .

We get:

Equation S3

$$R_c - R_{particle} = v_{DEP} \frac{w}{v_{flow}}$$

We can approximate  $v_{flow}$  to:

Equation S4

$$v_{flow} = \frac{\Delta P \cdot w^2}{24 \eta L}$$

Where  $\Delta P$  is the pressure across the device,  $w$  is the gap between posts,  $\eta$  is the viscosity and  $L$  the entire length of the device. The numerical factor in the denominator is determined taking into account the gap to depth ratio of 11/13.

To find an expression for the velocity due to the dielectrophoretic force, we need to consider the viscous drag and the dielectrophoretic force. The viscous drag force from a fluid of viscosity  $\eta$  on a sphere of radius  $r$  moving with a velocity  $v$  relative to the fluid is given by the Stokes drag:

Equation S5

$$F_{drag} = 6\pi\eta r v$$

The dielectrophoretic force  $F_{DEP}$  on the same size particle with complex permittivity  $\tilde{\epsilon}_p$  suspended in a medium with complex permittivity  $\tilde{\epsilon}_m$  and a sinusoidal electric field with an amplitude of  $E$  is given by

Equation S6

$$F_{DEP} = \pi \epsilon_m r^3 \text{Re}(f_{CM}) |\nabla E^2|$$

Combining Equations S5 and Equation S6 we have:

Equation S7

$$v_{DEP} = \frac{\epsilon_m \text{Re}(f_{CM}) R_{particle}^2 |\nabla E^2|}{6\eta}$$

We estimate a scaling relationship of the gradient.

Equation S8

$$|\nabla E^2| \propto \frac{1}{w} \frac{V^2}{w^2}$$

Here both the characteristic length scale of the gradient and the length scale over which the voltage is applied is set equal to the gap between the posts,  $w$ . Note that the voltage drop across the interface between the electrode and the electrolyte may be significant for small frequencies.

Neglecting any numerical prefactors, we can now combine the above equations to arrive at a scaling relationship for the cross-over voltage. Note that for polystyrene microspheres the conductivity is dominated by an essentially constant surface conductance. In the general case the Clausius-Mossotti factor,  $f_{CM}$ , is therefore expected to depend on the size of the particle [1]. However, at the high frequencies used in our experiments the permittivity dominates such that  $f_{CM} \sim -0.5$ . Thus,  $f_{CM}$  can be treated as a constant as a function of particle size.

Equation S9

$$V_c^2 \propto \frac{R_c - R_{particle}}{R_{particle}^2} \cdot \Delta P \cdot \frac{1}{\epsilon_m \text{Re}(f_{CM})} \cdot \frac{w^4}{L}$$

## 7. Data fitting

(a) Fitting to figure 4, error function fits to displacement vs. bead diameter

0V @ 10MHz

General model:

$$f(x) = a+d*(\text{erf}((x-b)/c) + 1)$$

Coefficients (with 95% confidence bounds):

$$\begin{aligned} a &= 7.928 \quad (7.681, 8.176) \\ b &= 6.159 \quad (6.004, 6.314) \\ c &= 0.8 \quad (\text{fixed at bound}) \\ d &= 2.883 \quad (2.579, 3.188) \end{aligned}$$

Goodness of fit:

SSE: 0.1585

R-square: 0.9948

Adjusted R-square: 0.9921

RMSE: 0.1991

1V @ 10MHz

General model:

$$f(x) = a+d*(\text{erf}((x-b)/c) + 1)$$

Coefficients (with 95% confidence bounds):

$$\begin{aligned} a &= 13.94 \quad (13.55, 14.33) \\ b &= 4.322 \quad (4.106, 4.537) \\ c &= -1.328 \quad (-1.904, -0.7517) \\ d &= -2.91 \quad (-3.17, -2.651) \end{aligned}$$

Goodness of fit:

SSE: 0.06228

R-square: 0.9986

Adjusted R-square: 0.9971

RMSE: 0.1441

2V @ 10MHz

General model:

$$f(x) = a+d*(\text{erf}((x-b)/c) + 1)$$

Coefficients (with 95% confidence bounds):

$$\begin{aligned} a &= 13.96 \quad (13.83, 14.09) \\ b &= 1.53 \quad (1.317, 1.742) \\ c &= -0.5291 \quad (-0.715, -0.3432) \\ d &= -3.168 \quad (-3.345, -2.992) \end{aligned}$$

Goodness of fit:

SSE: 0.02021

R-square: 0.9996  
 Adjusted R-square: 0.9993  
 RMSE: 0.08208

(b) Fitting to fig 6

$$f(x) = a+d*(\text{erf}((x-b)/c) + 1)$$

a=offset  
 b=mean  
 c=stdev  
 d=range/2

0.25 $\mu\text{m}$  beads:

General model:

$$f(x) = a+d*(\text{erf}((x-b)/c) + 1)$$

Coefficients (with 95% confidence bounds):

a = 8.925 (8.777, 9.073)  
 b = 9.146 (8.955, 9.337)  
 c = 3.016 (2.606, 3.427)  
 d = 2.415 (2.306, 2.524)

Goodness of fit:

SSE: 0.01724  
 R-square: 0.9994  
 Adjusted R-square: 0.999  
 RMSE: 0.06565

0.5 $\mu\text{m}$  beads:

General model:

$$f(x) = a+d*(\text{erf}((x-b)/c) + 1)$$

Coefficients (with 95% confidence bounds):

a = 7.561 (7.275, 7.847)  
 b = 5.62 (5.434, 5.806)  
 c = 0.9396 (0.6412, 1.238)  
 d = 3 (fixed at bound)

Goodness of fit:

SSE: 1.369  
 R-square: 0.9812  
 Adjusted R-square: 0.9774  
 RMSE: 0.37

*0.8 μm beads:*

General model:

$$f(x) = a+d*(\text{erf}((x-b)/c) + 1)$$

Coefficients (with 95% confidence bounds):

$$\begin{aligned} a &= 7.956 (7.728, 8.185) \\ b &= 3.491 (3.422, 3.56) \\ c &= 0.7239 (0.5923, 0.8556) \\ d &= 2.978 (2.84, 3.115) \end{aligned}$$

Goodness of fit:

SSE: 0.221

R-square: 0.9974

Adjusted R-square: 0.9965

RMSE: 0.1567

*2.1 μm beads:*

General model:

$$f(x) = a+d*(\text{erf}((x-b)/c) + 1)$$

Coefficients (with 95% confidence bounds):

$$\begin{aligned} a &= 7.945 (7.862, 8.029) \\ b &= 1.596 (1.578, 1.615) \\ c &= 0.3975 (0.358, 0.437) \\ d &= 3.024 (2.968, 3.079) \end{aligned}$$

Goodness of fit:

SSE: 0.01405

R-square: 0.9998

Adjusted R-square: 0.9997

RMSE: 0.053

*2.9 μm beads:*

General model:

$$f(x) = a+d*(\text{erf}((x-b)/c) + 1)$$

Coefficients (with 95% confidence bounds):

$$\begin{aligned} a &= 7.645 (7.605, 7.685) \\ b &= 1.333 (1.325, 1.341) \\ c &= 0.4614 (0.4474, 0.4753) \\ d &= 3.174 (3.15, 3.198) \end{aligned}$$

Goodness of fit:

SSE: 0.002181

R-square: 1

Adjusted R-square: 0.9999  
RMSE: 0.02089

*4.3 μm beads:*

General model:

$$f(x) = a + d * (\text{erf}((x-b)/c) + 1)$$

Coefficients (with 95% confidence bounds):

$$\begin{aligned} a &= 7.763 \quad (7.534, 7.992) \\ b &= 1.006 \quad (0.9654, 1.046) \\ c &= 0.6021 \quad (0.5251, 0.6791) \\ d &= 3.121 \quad (2.989, 3.253) \end{aligned}$$

Goodness of fit:

SSE: 0.02156  
R-square: 0.9996  
Adjusted R-square: 0.9992  
RMSE: 0.07342

*6.1 μm beads:*

General model:

$$f(x) = a + d * (\text{erf}((x-b)/c) + 1)$$

Coefficients (with 95% confidence bounds):

$$\begin{aligned} a &= 7.584 \quad (6.518, 8.651) \\ b &= 0.2 \quad (\text{fixed at bound}) \\ c &= 1.082 \quad (0.6235, 1.541) \\ d &= 3.33 \quad (2.492, 4.169) \end{aligned}$$

Goodness of fit:

SSE: 0.8462  
R-square: 0.9421  
Adjusted R-square: 0.9276  
RMSE: 0.3252

*(c) Fitting to figure 8A, crossover as function of square root of pressure (max displacement – channel 14):*

Linear model Poly1:

$$f(x) = p1 * x + p2$$

Coefficients (with 95% confidence bounds):

$$\begin{aligned} p1 &= 0.8289 \quad (0.8161, 0.8418) \\ p2 &= -0.2017 \quad (-0.2689, -0.1344) \end{aligned}$$

Goodness of fit:

SSE: 0.02211  
R-square: 0.9994  
Adjusted R-square: 0.9993  
RMSE: 0.04292

(d) Fitting to figure 8A, crossover as function of square root of pressure (crossover displacement – channel 11):

Linear model Poly1:

$$f(x) = p1 * x + p2$$

Coefficients (with 95% confidence bounds):

$$p1 = 0.5886 \text{ (0.5682, 0.6091)}$$

$$p2 = -0.2027 \text{ (-0.3123, -0.09309)}$$

Goodness of fit:

SSE: 0.03802

R-square: 0.9979

Adjusted R-square: 0.9977

RMSE: 0.065

(e) Fitting to figure 8B, fit with  $R_c=3.0785$  (from error function fit to displacement  $v$  diameter plot, figure 4)

Linear model Poly1:

$$f(x) = p1 * x + p2$$

Here we use the part of equation (4) that describes the particle size as follows:

$$x = \sqrt{\frac{R_c - R_{part}}{R_{part}^2}}$$

Coefficients (with 95% confidence bounds):

$$p1 = 0.6548 \text{ (0.5678, 0.7419)}$$

$$p2 = 0.5632 \text{ (0.07268, 1.054)}$$

Goodness of fit:

SSE: 1.221

R-square: 0.9826

Adjusted R-square: 0.9797

RMSE: 0.451

## 8. Switching time

In order to determine the results of a separation as parameters are tuned, short response times are preferable. Figure S 8 shows the time evolution of particle distributions at the outlet of the device after the applied voltage is switched from 0 Vpp to 7.5 Vpp at time  $t = 0$ . The separation is fully developed after 4 s. The mean velocity of 2.1  $\mu\text{m}$  microspheres was measured at  $\sim 250 \mu\text{m s}^{-1}$  @ 3mBar. With the velocity proportional to the applied pressure

this would mean  $0.75 \text{ mm s}^{-1}$  @ 10 mBar which is comparable to 4.6 mm in 4 s. In other words, the switching time is simply related to the time it takes particles to traverse the device.

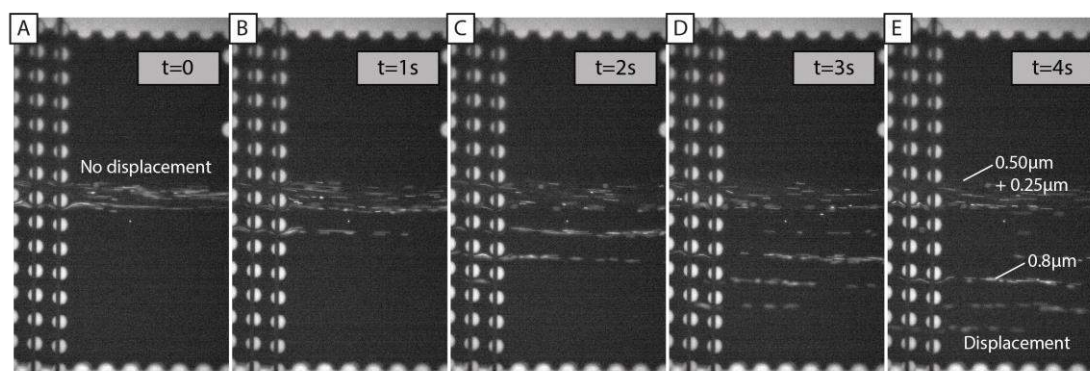


Figure S 8. At  $t=0$  the 7.5 Vpp @ 10 MHz is applied. The response is immediate, and the separation fully developed at 4 s. Measurement performed at 10 mBar where the displacement is less than that shown in previous results (3 mBar).

## 9. Videos

A selection of videos of the results are available at <http://bit.ly/MetalDLDVideos>.

The following first four movies show tunable sorting (**Error! Reference source not found.** is taken from here). The applied pressure is 3 mBar, frequency is 10 Mhz. The 250 nm and 500 nm microspheres are green, and the 800 nm microspheres are red. Movies are played back at half speed. The first four movies with the respective applied voltages:

active posts Supporting Information movie1: 0 Vpp

active posts Supporting Information movie2: 3.5 Vpp

active posts Supporting Information movie3: 5.25 Vpp

active posts Supporting Information movie4: 7 Vpp

The fifth movie shows switching. The applied pressure is 10mBar, frequency is 10Mhz. 250 nm and 500 nm and 800 nm microspheres are all visible at the beginning of the movie. Movie is played back at actual speed. The applied voltage in the beginning of the movie is 0 Vpp and is switched to 7 Vpp at 1 s. At 15 s the excitation light is switched so that the

800 nm microspheres only are visible. Then at 16 s switched again so that the 250 nm and the 500 nm microspheres only are visible.

active posts Supporting Information movie5: 0 Vpp – 7 Vpp

## 10. References

[1] Ermolina, I. and H. Morgan, The electrokinetic properties of latex particles: comparison of electrophoresis and dielectrophoresis. *Journal of Colloid and Interface Science*, 2005. 285(1): p. 419-428.